Modeling Bottom Mixed Layer Variability on the Mid-Oregon Shelf during Summer Upwelling

A. L. KURAPOV, J. S. ALLEN, G. D. EGBERT, AND R. N. MILLER

College of Oceanic and Atmospheric Sciences, Oregon State University, Corvallis, Oregon

(Manuscript received 2 July 2004, in final form 10 February 2005)

ABSTRACT

Results from a model of wind-driven circulation are analyzed to study spatial and temporal variability in the bottom mixed layer (BML) on the mid-Oregon shelf in summer 2001. The model assimilates acoustic Doppler profiler velocities from two cross-shore lines of moorings 90 km apart to provide improved accuracy of near-bottom velocities and turbulence variables in the area between the mooring lines. Model results suggest that the response of the BML thickness to upwelling- and downwelling-favorable winds differs qualitatively between an area of "simple" bathymetric slope at 45°N and a wider shelf area east of Stonewall Bank (44.5°N). At 45°N, the BML grows in response to downwelling-favorable conditions, in agreement with known theories. East of Stonewall Bank, the BML thickness is increased following upwelling events. In this area, the southward upwelling jet detaches from the coast and flows over a wider part of the Oregon shelf, creating conditions for Ekman pumping near the bottom. Based on computations of bottom stress curl, the vertical pumping velocity in this area may reach 15 m day^{-1} following periods of intensified upwelling-favorable winds. A column of denser, near-bottom water upwelled over the Ekman flow convergence area is tilted as a result of vertical shear in horizontal velocities, causing unstable stratification and convective overturning. As a result of this process, BML thickness values east of Stonewall Bank can be in excess of 20 m following upwelling, comparable to maximum values at 45°N following downwelling.

1. Introduction

Understanding spatial and temporal variability in the near-bottom mixing on the shelf is important; for example, it results in the suspension of nutrient-rich sediments, which then can be upwelled into the euphotic zone to support phytoplankton growth (Chase et al. 2002). In many shallow regions, bottom mixing depends on the wind forcing. Observational studies of bottom mixed layer (BML) variability on the shelf slope reveal that the BML is thicker in response to downwelling-favorable conditions and thinner during upwelling (Lentz and Trowbridge 1991). Idealized theoretical models (Trowbridge and Lentz 1991; MacCready and Rhines 1993; Garrett et al. 1993) relate this effect to the cross-shore Ekman buoyancy transport. During upwelling, dense water moves upslope, resulting in increased stratification near the bottom that limits vertical mixing to a small bottom boundary layer (BBL). During downwelling, the situation is reversed, with weakened stratification and enhanced turbulence near the bottom. Lentz and Trowbridge (1991) discussed the possibility of convective instability as the source of enhanced BBL mixing during downwelling, as the downslope bottom Ekman transport is carrying lighter water under heavier water. Further details of this convective process have recently been described based on turbulence microstructure measurements (Moum et al. 2004).

Over complicated shelf bathymetry, a variety of mechanisms may cause enhanced near-bottom mixing, besides the one mentioned above. For example, analysis of measurements over Stonewall Bank on the Oregon shelf (44.5°N, 124.4°W; Fig. 1a) has shown that enhanced turbulence and mixing can be associated with hydraulically controlled flow over this small topographic feature (Nash and Moum 2001).

Present observational programs have difficulty providing adequate spatial and temporal coverage of the

Corresponding author address: Dr. Alexander Kurapov, COAS, Oregon State University, 104 COAS Admin. Bldg., Corvallis, OR 97331-5503.
E-mail: kurapov@coas.oregonstate.edu

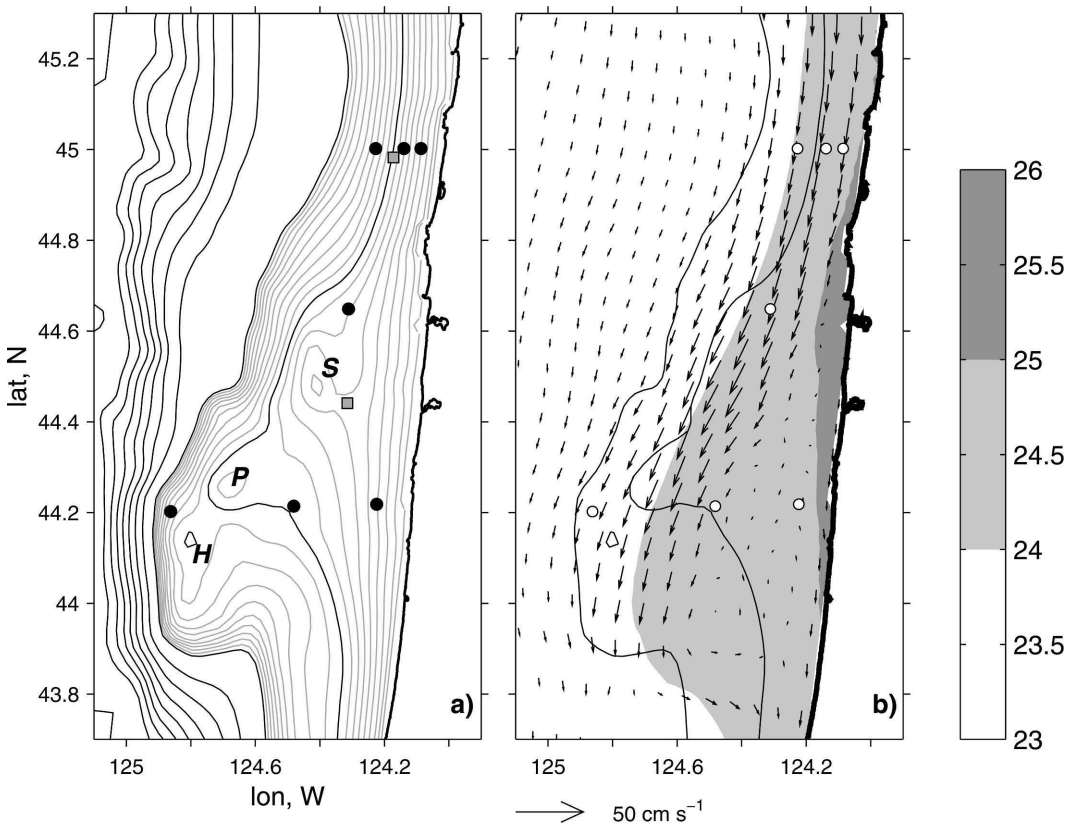

FIG. 1. (a) Map of mid-Oregon shelf. Bathymetric contour intervals are 100 m for the black lines and 10 m (from 10 to 200 m) for the half-tone lines. Circles show mooring locations. Labels S, P, and H denote banks: Stonewall, Perpetua, and Heceta. Square symbols mark locations for which time series of bottom variables are shown in Fig. 4. (b) Time- and depth-averaged current and time-averaged potential density σ_θ at the surface, days 146–191, 2001. Velocity vectors are shown at each third grid point. Bathymetric contours are 100 and 200 m.

processes in the BBL over complicated shelf bathymetry. At the same time, numerical models based on fully nonlinear primitive equations and incorporating comprehensive turbulent parameterization schemes have reached a sufficient degree of realism such that they can be useful for the analysis of the BBL processes in three spatial dimensions and time (Kurapov et al. 2005b). These models can be utilized to identify times and locations of energetic mixing and then to study driving mechanisms.

In this paper, a data-assimilative model of coastal wind-driven circulation (Kurapov et al. 2005a,b) is utilized to study spatial and temporal variability in BBL processes on the mid-Oregon shelf. The motivation for this study is to verify whether variability in the BML thickness in the numerical model is consistent with the above-mentioned theoretical models. Unexpectedly, we find that the response of the BML thickness to upwelling- and downwelling-favorable winds is qualitatively different in an area of a relatively narrow shelf with weak alongshore topography variations (45°N) and an area of wider shelf east of Stonewall Bank (44.5°N).

Despite a history of observational studies on the Oregon shelf, direct measurements have provided limited information about temporal and spatial variability in the BML in that region. From an 8-day sequence of turbulence microstructure transects made at 45°N in May–June 2001, Perlin et al. (2005) found that the BML thickness in that area was larger in response to the relaxation of upwelling winds. During the same cruise, events of large BML thickness were also observed southeast and northeast of Stonewall Bank in single turbulence microstructure transects at 44.38° and 44.55°N (A. Perlin 2004, personal communication). Barth et al. (2005) also report about layers of low near-bottom stratification over the bank summit and on the inshore side of the bank, observed in the SeaSoar conductivity–temperature–depth (CTD) hydrographic sections in July 1999. At the time of those observations, the core of the upwelling jet was located on the offshore side of Stonewall Bank.

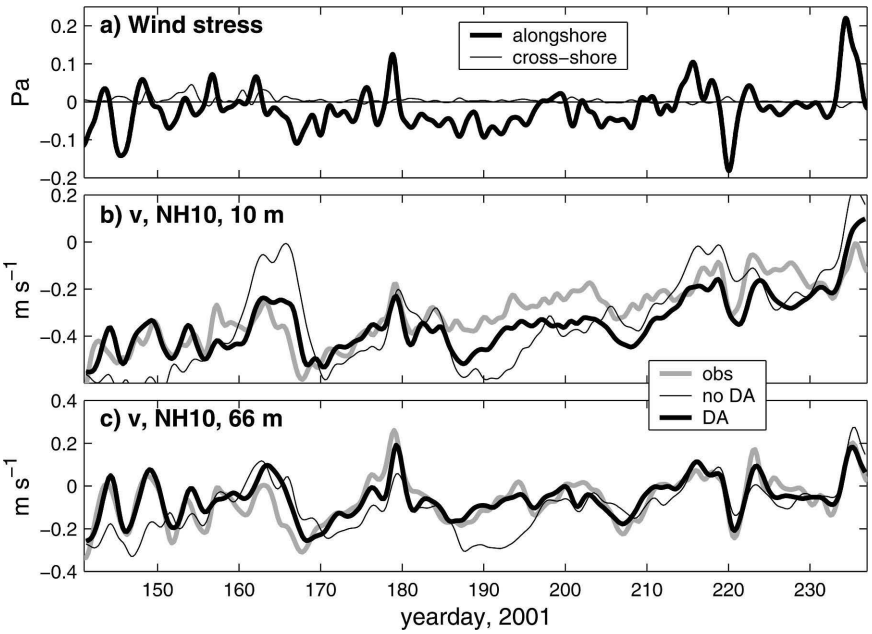

FIG. 2. Time series of (a) wind stress, (b) alongshore velocity component v at NH10 mooring location (44.65°N) at 10 m below sea surface (moored profiler observations are gray, the no-DA solution is the thin line, and the DA solution is the thick black line), and (c) same as (b), but at 66 m below sea surface (15 m above the bottom).

The paper is organized as follows. The model description is given in section 2. An overview of the summer upwelling regime off Oregon including analysis of near-bottom horizontal currents and stresses is found in section 3. The qualitatively different responses of the BML to upwelling and downwelling conditions in the area of the narrow shelf (45°N) and east of Stonewall Bank (44.5°N) are analyzed in section 4. Possible implications of the studied process east of Stonewall Bank for the circulation and biological variability in the area are discussed in section 5, and a summary is given in section 6.

2. Data-assimilative model

The dynamics are based on the Princeton Ocean Model (POM; Blumberg and Mellor 1987), a fully nonlinear, free-surface, hydrostatic model with a subgrid turbulence parameterization scheme (Mellor and Yamada 1982; Galperin et al. 1988). The model configuration is similar to that used in Oke et al. (2002a,b,c) and Kurapov et al. (2005a,b). The model domain extends 220 km offshore and 350 km alongshore. The grid is rectangular with the horizontal (x, y) axes rotated 7° clockwise from north. The x axis is then directed cross-shore, toward the coast, and the y axis is directed alongshore, positive to the north. Velocity components in these directions are u and v, respectively. Horizontal grid resolution is near 2 km in the central part of the model domain, over the mid-Oregon shelf (Fig. 1a). The model uses terrain-following coordinates in the vertical, with 45 σ layers, including 8 concentrated near the surface and 4 near the bottom in order to resolve boundary layers. Alongshore boundary conditions are periodic, with the bathymetry and coastline smoothed and matched near the south and north ends of the domain (beyond the limits of the map in Fig. 1a). Extensive model–data comparisons (Oke et al. 2002a,b; Kurapov et al. 2005a,b) have shown that POM in this periodic configuration is capable of reproducing a substantial fraction of the observed variance of the wind-driven alongshore currents on the shelf in this region. That success evidently follows from the fact that Oregon shelf flows are strongly driven by local winds and dominated by flow–topography interactions.

The model is forced with alongshore wind stress and surface heat flux. Atmospheric parameters for the calculation of the surface fluxes were measured at a meteorological buoy located midshelf at latitude 45°N. In the model, these inputs are assumed to be spatially uniform. Since our focus is on subinertial wind-forced ocean variability, the wind stress (Fig. 2a) and the measured variables used for heat flux computation are low-pass filtered with half-amplitude cutoff of 40 h. The

mooring data used for assimilation are also low-pass filtered.

Other model details, including description of initial conditions and the spinup, can be found in Kurapov et al. (2005b). The analysis period starts on day 146 (26 May) of 2001, after the model has been spun up from rest for 23 days, and extends to day 237 (25 August), covering most of the summer upwelling season.

In the course of this study, we analyzed both the model solution without data assimilation (DA) and a solution constrained by assimilation of velocities from two cross-shore lines of moored acoustic Doppler profilers, at 45°N (line N) and 44.2°N (line S). Mooring locations are shown in Fig. 1a. The moorings at these two lines were part of the Coastal Ocean Advances in Shelf Transport (COAST) project (Boyd et al. 2002). At these moorings, time series of horizontal velocity measurements were obtained in 2- or 4-m vertical bins as close as 9–15 m to the sea surface and bottom [for instrument characteristics see, e.g., Table 1 in Kurapov et al. (2005a)]. The data are assimilated using an optimal interpolation algorithm that provides sequential correction to the model horizontal velocities based on model–data differences. This DA method requires a time-invariant estimate of the forecast error covariance (see Kurapov et al. 2005a). Other prognostic variables are not corrected as a part of the data assimilation scheme, but are allowed to adjust dynamically to the velocity corrections. Assimilation is done every one-quarter of an inertial period, approximately 4.2 h. To inhibit spurious high-frequency oscillations caused by imposed, instantaneous changes in the velocity fields, an incremental approach is taken, such that the correction is applied gradually over the analysis window.

In this study, unless specified, results from the data assimilation solution are presented. Assimilation of velocities from lines S and N has been shown to improve not only model velocities in the area between these lines, but also a number of other oceanic variables of interest such as the sea surface height, temperature, and potential density (Kurapov et al. 2005b). Most relevant here, comparison of DA and model-only (no DA) solutions with turbulence microstructure measurements from a 8-day series of transects at 45°N (Moum et al. 2004) has shown that moored velocity DA provides improvement in the level of the near-bottom turbulent dissipation rate and the bottom stress during upwelling. In spite of those improvements, the DA solution should be analyzed with some caution since the corrected fields are only in approximate dynamical balance (Kurapov et al. 2005a). Note, however, that except for the momentum equations, all the other model equations are satisfied exactly, since only horizontal velocities are corrected by means of data assimilation and other fields are adjusted dynamically. In particular, this facilitates the term balance analysis in the temperature equation in section 4. Since the stationary forecast error covariance used in the DA algorithm is representative of the average upwelling situation, the accuracy of the DA solution is possibly better in response to southward, upwelling-favorable winds than to northward, downwelling-favorable wind events. Aware of these limitations of DA, we have verified that all qualitative effects discussed below are present in both the model only and the DA solutions. The effect of data assimilation is to correct the spatial and temporal intensity of the processes under consideration, but not to alter the dominant dynamical features.

3. Summer circulation regime off Oregon

The predominantly southward wind stress (Fig. 2a) forces a time-averaged southward alongshore current that is accompanied by upwelling of density surfaces near the coast. Figure 1b shows the time-averaged (days 146–191) depth-averaged current and the time-averaged potential density σ_θ at the surface from the DA run. Near latitude 44.8°N, where the shelf widens, the upwelling jet detaches from the shore. Flowing over the wider shelf region including Stonewall Bank (44.5°N), Perpetua Bank (44.25°N), and Heceta Bank (44.15°N), the energetic current crosses isobaths and separates from the shelf, where the shelf narrows again. Contours of the time-averaged σ_θ at the surface generally follow time- and depth-integrated current streamlines, with a wider area of upwelled water near mooring line S than near line N.

Assimilation of velocities from moorings on lines N and S improves velocity prediction at mooring NH10 [a part the Global Ocean Ecosystem Dynamics (GLOBEC) program], located in the middle of the observational array at 44.65°N, in the 81-m-deep water (see Fig. 1a). Time series of observed and modeled (with and without DA) alongshore velocities v are shown in Fig. 2 for the uppermost (10 m) and lowest (66 m) profiler bins. At 10 m below the sea surface, the model–data rms error is improved from 12.7 to 8.2 cm s^{-1} as a result of DA, and the amplitude of complex correlation (defined as a correlation of complex time series $u + iv$) increased from 0.58 to 0.70. At 66-m depth, the model–data rms error is improved from 8.1 to 4.4 cm s^{-1}, and the amplitude of complex correlation from 0.52 to 0.83. Kurapov et al. (2005a) discuss model deficiencies in the second part of the study period, when the model does not reproduce significant frontal

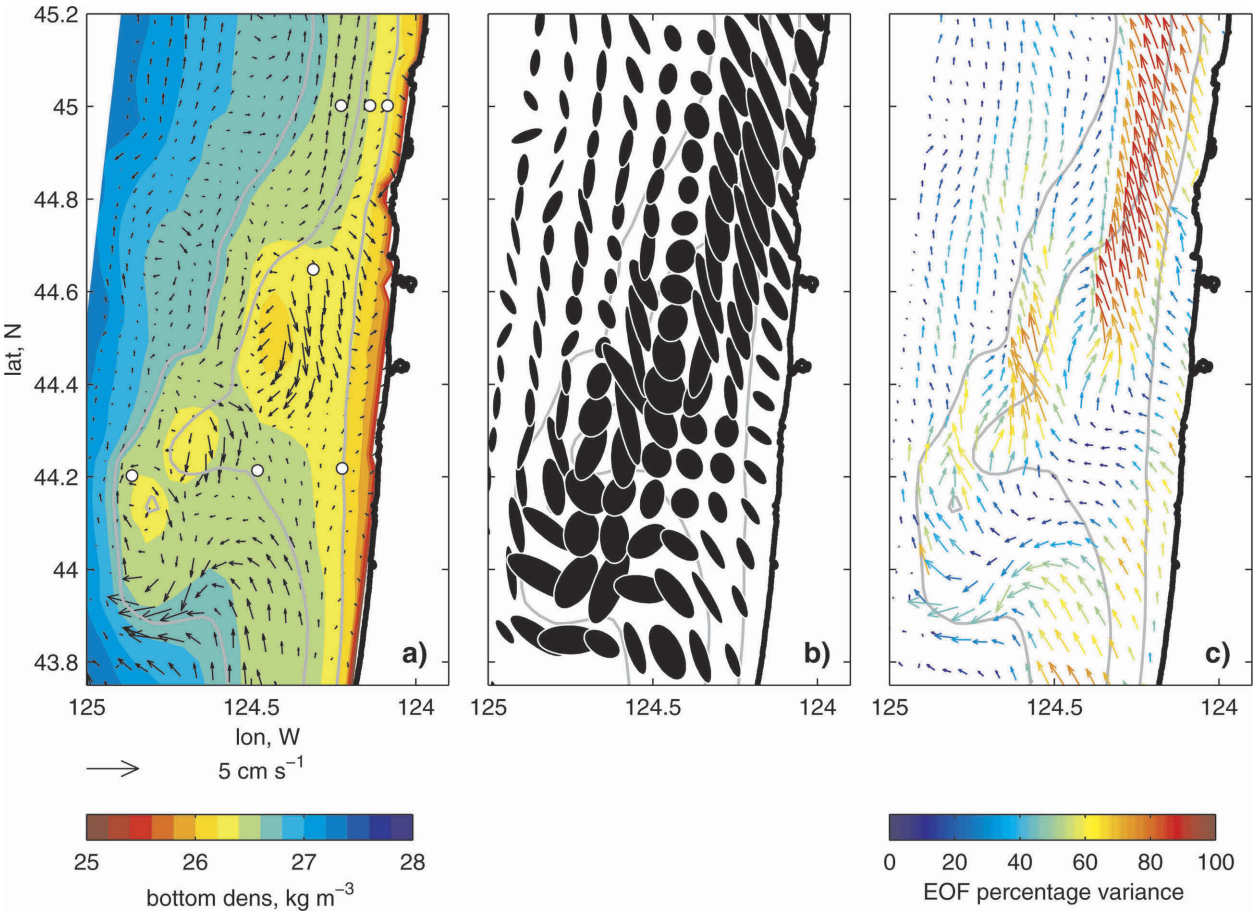

FIG. 3. Statistics of the horizontal current near bottom, days 146–237: (a) time-averaged bottom current (vectors) and potential density (color), (b) std dev ellipses of the bottom current [scale is the same as that for vectors in (a)], and (c) first EOF of bottom currents, explaining on average 52% of the total variance; color shows the percentage variance explained locally by this EOF. Vectors are shown at each second grid point, and variance ellipses at each fourth grid point. Bathymetric contours are 50, 100, and 200 m. Circles show mooring locations.

fluctuations apparent in satellite SST images. During this time, the southward model currents can be noticeably larger than observed. This problem is evident at the NH10 site 10 m below the sea surface, especially during days 185–215 (even in the DA solution, Fig. 2b). However, close to the bottom, the model current from the DA solution is close to observations for the whole study period (Fig. 2c). This gives us confidence in analyzing the near-bottom dynamics using the DA solution for the entire study period (days 146–237). Based on encouraging model–data comparisons with respect to the turbulent microstructure data mentioned in section 2 and on our understanding that improvement in near-bottom turbulent quantities is associated with correction of velocities near the bottom, we may expect that BBL variability is improved in the entire region between the mooring lines, since velocities are constrained by data assimilation on lines N and S and significant improvement in (u, v) is verified to be obtained at NH10.

The near-bottom dynamics are dominated by upwelling/downwelling processes and flow interactions with local bathymetric features, as seen in maps of time averages, standard deviation ellipses and the first EOF computed for bottom velocity fields (Fig. 3). The color of the EOF vectors corresponds to the percentage of the total velocity variance explained locally by this EOF. The temporal coefficient of the first EOF is positively correlated with the wind stress (correlation coefficient 0.61), such that the spatial pattern in the EOF plot (Fig. 3c) is characteristic of downwelling.

Over the midshelf in the area north of 44.8°N, the mean currents are small relative to their standard deviations. Polarization and orientation of the standard deviation ellipses can be explained here by the dynamics of upwelling/downwelling on the slope. The first

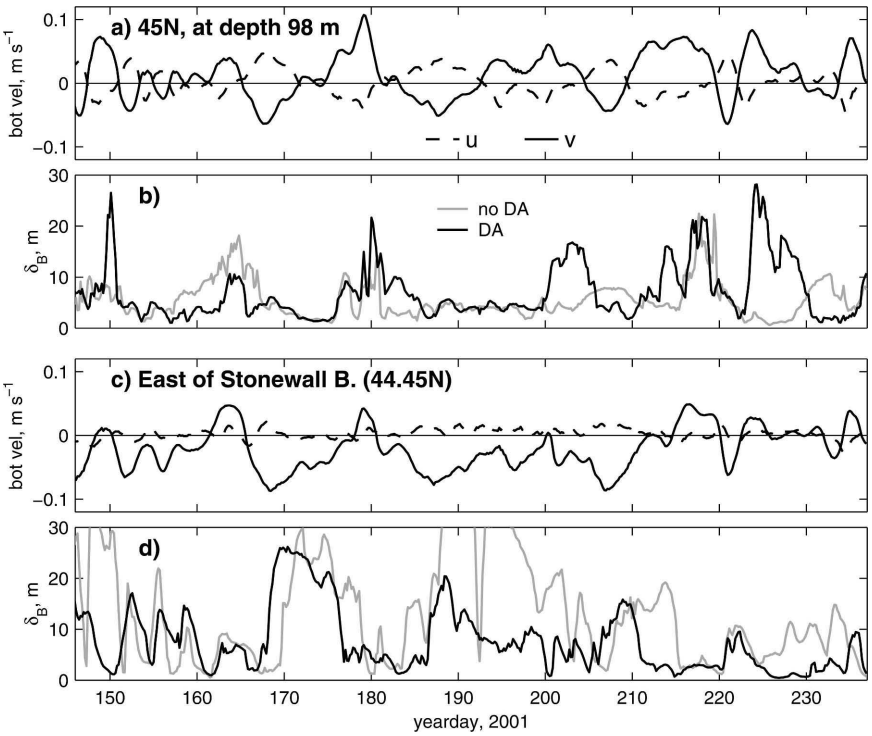

FIG. 4. Time series of (a) bottom velocity at the location marked in Fig. 1 near latitude 45°N, cross-shore (dashed line) and alongshore (solid line) components and (b) the BML thickness at the same location, the no-DA (gray), and DA (black) solutions. (c), (d) Analogous to (a) and (b), respectively, but shown for a location east of Stonewall Bank, marked in Fig. 1 at 44.45°N.

EOF explains over 80% of the variance in bottom currents in this area, such that an estimate of the bottom current in response to upwelling (downwelling) conditions can be approximated well by the mean minus (plus) the scaled first EOF. Here, the bottom currents change direction in response to the change in the wind direction. The northward and southward currents are of comparable amplitude as can be seen, for instance, in a time series plot of the bottom current (u, v) at a midshelf location at 45°N (Fig. 4a).

On the midshelf east of Stonewall Bank (44.5°N), the bottom current is southward on average, with magnitudes near 4 cm s^{-1}. In this area, the first EOF also explains a large percentage of the bottom velocity variance. During upwelling, the southward current is intensified. During downwelling, it is weakened, but not always reversed (see, e.g., Fig. 4c showing a time series of the bottom current at a location east of Stonewall Bank). Northward currents in response to downwelling-favorable conditions are generally weaker than southward currents at this location.

In the model, a significant mean bottom current is also seen near 44.4°N, between Stonewall and Perpetua Banks (see Fig. 3a), which tends to carry dense water around Perpetua Bank. A relatively large, mean northward bottom current is found on the continental slope southeast of Heceta Bank (44.0°N). The depth-integrated momentum term balance analysis of Gan and Allen (2005) shows that the northward bottom stress associated with this current is typically balanced by an ageostropic pressure gradient term resulting from flow over alongshore-varying bathymetry. A weak (1–2 cm s^{-1}) northward near-bottom current near latitude 45°N may also be noticed over bathymetric depths $H >$ 80 m (see Fig. 3a). It is evidently driven by a similar mechanism, resulting from the offshore deflection of the alongshore current over a relatively wider shelf north of 45°N and its subsequent reattachment near 45°N. A northward current of 1–2 cm s^{-1} is also found in measurements of horizontal velocities from the midshelf mooring (45°N, 81-m depth) at the distance of 2–10 m from the bottom, averaged over days 146–237.

In the area between Stonewall and Heceta Banks standard deviation ellipses are less polarized than in the area of simple bathymetric slope. The first EOF explains a low percentage of variability there. The plot of the amplitude of the complex correlation between the bottom horizontal current and the wind stress (Fig. 5)

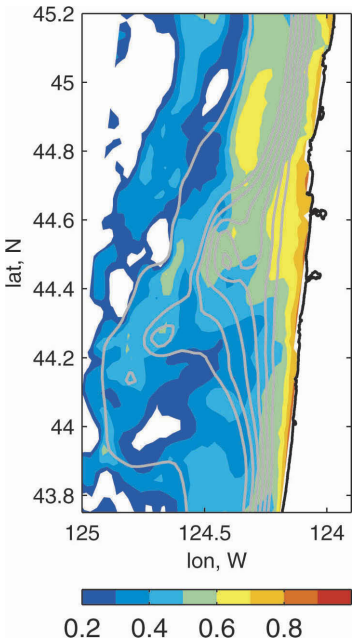

FIG. 5. Amplitude of complex correlation between the bottom horizontal current and wind stress, days 146–237. Bathymetric contours are from 50 to 100 m (every 10 m), and 200 m.

indicates that variability in the bottom velocities in the area over the banks is less tied to variability in the wind than in the area of the inner shelf ($H < 50$ m) and of the entire shelf north of Stonewall Bank.

Contours of the time-averaged bottom σ_θ (colors in Fig. 3a) are generally aligned with bathymetry, with an exception in a region around 44.7°N, near the northern tip of Stonewall Bank, where the 26.4 kg m^{-3} isopycnal is seen to cross bathymetric contours in the range of depths between 70 and 120 m.

It is also useful to document the spatial and temporal variability in the bottom stress vector field $\boldsymbol{\tau}_B = [\tau_B^{(x)}, \tau_B^{(y)}]$ because of its importance for bottom mixing. The time-averaged τ_B, its standard deviation ellipses, and the first EOF are shown in Fig. 6. Again, the first EOF temporal amplitude coefficient is positively correlated with the wind stress (correlation coefficient 0.58). This EOF explains a large fraction of modeled variability in τ_B in the same areas as the bottom velocity first EOF. The color contours in Fig. 6a show the magnitude of the time-averaged stress, with larger values along the path of the upwelling jet over the area of complicated bathymetry and in the recirculation area southeast of Heceta Bank. The time-averaged bottom stress near mooring line N is relatively low, although significant variability is predicted in response to upwelling/downwelling conditions (Fig. 6b). In the area east of Stonewall Bank (44.5°N), at midshelf depths (>50 m), the bottom stress is large on average and it increases in response to upwelling conditions. However, at the same latitude, both the mean and the standard deviation of τ_B are low on the inner shelf (depths < 50 m). This suggests an area of increased bottom stress curl, resulting in the cross-shore bottom Ekman transport convergence discussed below.

4. Qualitatively different BML response to wind conditions at 45°N and in the area east of Stonewall Bank (44.5°N)

In this study, the BML thickness δ_B is defined analogous to Moum et al. (2004) as the distance from the bottom over which the potential density σ_θ decreases by $\Delta\sigma_\theta = 0.0006$ kg m^{-3} from its bottom value. In Moum et al. (2004), this specific value of $\Delta\sigma_\theta$ was chosen based on analysis of a series of measured density profiles on the Oregon shelf. Although the choice of $\Delta\sigma_\theta$ is subjective, δ_B defined in this way is suitable for comparative description of the BML thickness at different times and locations on the shelf. In our model, the bottom σ_θ is determined from the lowest σ layer, at a location one-half of a grid cell above the bottom. For instance, in our case, the lowest density layer is 0.34 m above the bottom in 100-m-deep water. Since the vertical resolution in this model is proportional to the bathymetric depth $H(x, y)$, it is limited in deep areas. For this reason, δ_B is analyzed here only for $H < 200$ m.

Solution analysis reveals several areas where δ_B can be high, with values in excess of 20 m, for instance, on the narrow shelf at 45°N, east of Stonewall Bank (44.5°N), in the passage between Stonewall and Perpetua Banks (44.4°N) and in the area near the southern flank of Heceta Bank (43.9°N). Our study is focused on the BML behavior between the two mooring lines, at 44.2° and 45°N, in the area where the model has been more thoroughly verified (Kurapov et al. 2005a,b). Analysis of variability in the BML near Heceta Bank may be important for understanding biological productivity in that area, but is not pursued, as we lack the time series measurements to validate model accuracy there.

Time series of δ_B at two midshelf locations (marked as gray boxes in Fig. 1a) are shown in Figs. 4b (for the location at 45°N) and 4d (for the location east of Stonewall Bank, at 44.5°N). In these plots, black lines correspond to the DA solution, and half-tone lines to the model solution without DA. Information on whether an event of large mixing is associated with upwelling ($u > 0, v < 0$) or downwelling ($u < 0, v > 0$) is provided by plots of the bottom horizontal velocity components at the corresponding locations (Figs. 4a,c). At both lo-

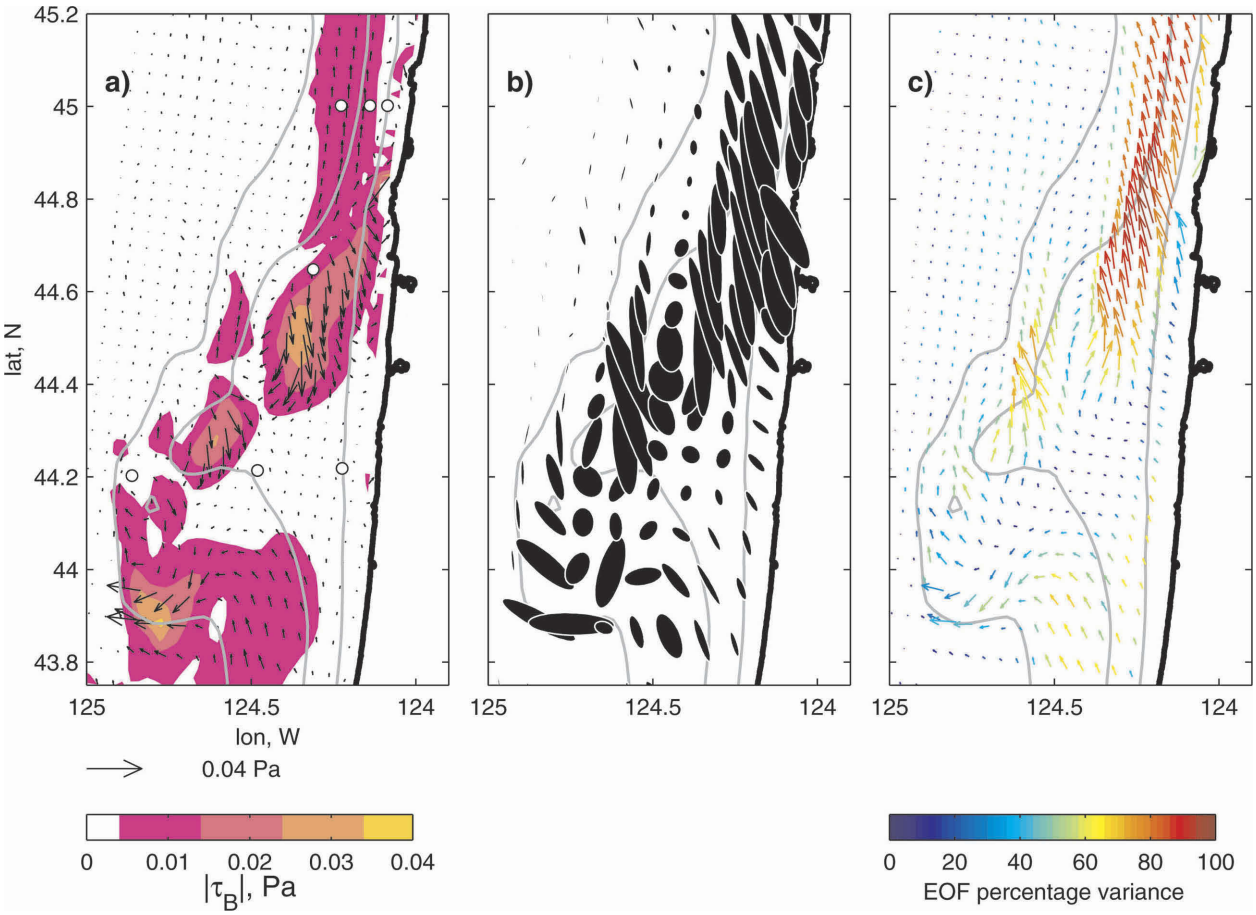

FIG. 6. Bottom stress statistics for days 146–237: (a) time-averaged (color background shows the magnitude of τ_B), (b) std dev ellipses, scaled similar to vectors in (a), and (c) first EOF, explaining on average 66% of the total variance; color shows the percentage variance explained locally by this EOF. Vectors are shown at each second grid point, and variance ellipses at each fourth grid point. Bathymetric contours are 50, 100, and 200 m. Circles show mooring locations.

cations, the model predicts events of large δ_B. Assimilation of moored velocities modifies not only mixing intensity, but also the time of occurrence of the mixing events.

Careful comparison of Figs. 4b and 4d reveals that periods of large δ_B at 45°N occur when δ_B is small at the location east of Stonewall Bank, and vice versa. This can be seen clearly in a scatter diagram, where δ_B values at one location are plotted against those at the other (Fig. 7). As discussed in section 1, δ_B at 45°N is expected to be larger in response to downwelling conditions. This relationship is clearly evident in the scatter diagram of Fig. 8a, with bottom u and v on the axes and different symbols corresponding to different ranges of δ_B. In this plot, points are sorted according to δ_B such that points in a higher δ_B range overlay those in a lower range. Clearly, at 45°N, events of large δ_B occur when the bottom current is directed offshore and to the north. Solution analysis confirms that increased δ_B at 45°N is associated with downslope buoyancy transport, as outlined in section 1. In contrast, the u–v scatter diagram for the location east of Stonewall Bank (Fig. 8b) shows larger δ_B during periods of increased southward current, in response to upwelling-favorable conditions.

To explain the BML behavior east of Stonewall Bank, we look in more detail at the upwelling event on days 165–171 (see Fig. 2a) when δ_B in this area becomes the largest over the entire study period. During this event, the southward wind stress reaches its maximum magnitude on day 167.1. The time of maximum southward bottom velocity comes later, on day 168.5 (see Fig. 4c). During this time, the BML thickness shows intensive growth (see Fig. 4d) approaching its largest value on day 169.5. The BML thickness east of Stonewall Bank (44.5°N) is relatively small in the beginning of this upwelling event, as seen in the map of δ_B averaged over day 166 (Fig. 9a). However, in a similar map for day 170

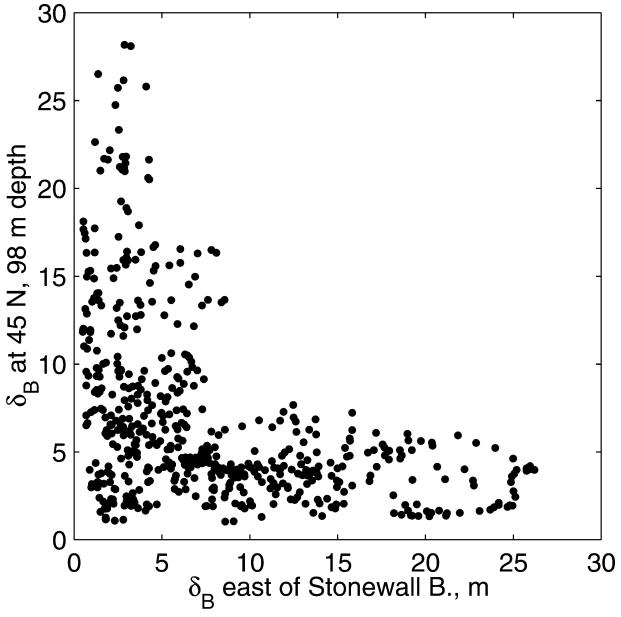

FIG. 7. Scatter diagram of δ_B at 45°N (shown as a time series in Fig. 4b) vs δ_B east of Stonewall Bank (shown as a time series in Fig. 4d), days 146–237.

(Fig. 9b) the BML thickness east of Stonewall Bank is >12 m in an area stretching 45 km alongshore, with the maximum values in excess of 30 m southeast of the bank. At the same time, near latitude 45°N, $\delta_B < 4$ m. Mixing is also low all along the 100-m isobath west of Stonewall and Perpetua Banks. In contrast, on day 180 following a downwelling wind event, δ_B attains its maximum value at 45°N and is relatively small δ_B east of the banks (Fig. 9c).

The following mechanism is proposed to explain variability in δ_B east of Stonewall Bank. The alongshore jet is detached from the coast and flows over the wide shelf south of 44.8°N creating conditions for bottom Ekman transport convergence inshore of the jet core. Ekman pumping resulting from that convergence can upwell a column of dense fluid over the midshelf. This upwelled structure can then be tilted as a result of the vertical shear in the horizontal velocity, advecting dense upwelled water over lighter surrounding water and setting up conditions for convective mixing.

To verify this hypothesis, which would explain the large δ_B in response to upwelling conditions east of Stonewall Bank, we first quantify the intensity of the bottom Ekman pumping by computing a "pumping velocity," which is proportional to the curl of the bottom stress:

$$w_p = \frac{\text{curl}\,\tau_B}{\rho_o f} = \frac{1}{\rho_o f}\left[\frac{\partial \tau_B^{(y)}}{\partial x} - \frac{\partial \tau_B^{(x)}}{\partial y}\right], \qquad (1)$$

where ρ_o is the reference density and f is the Coriolis parameter. Following boundary layer analysis similar to Pedlosky (1987, his section 4.10), it can be shown that w_p (1) is a BBL correction to the interior vertical velocity at the top of the BBL.

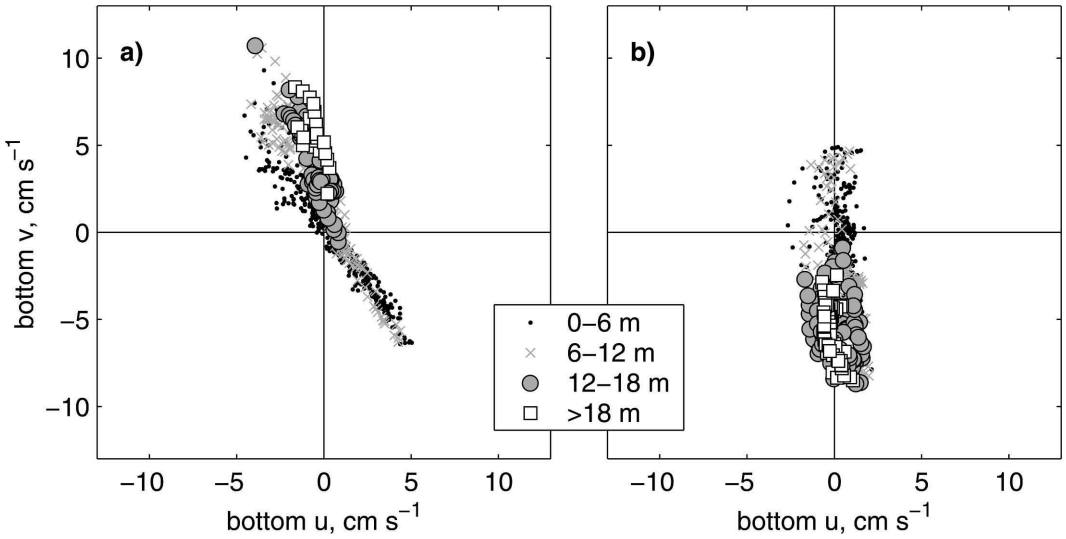

FIG. 8. Bottom u–v scatter diagrams showing dependence of the BML thickness δ_B on the direction and magnitude of the bottom current. Axes are the cross-shore (u) and alongshore (v) bottom current components (in the coordinate system rotated 7° clockwise from the true north). The magnitude of δ_B is shown with different symbols. Points are plotted in the order corresponding to the magnitude of δ_B, such that points in a higher δ_B range overlay those in a lower δ_B range: (a) middepth location at 45°N, (b) location east of Stonewall Bank (these locations are marked in Fig. 1).

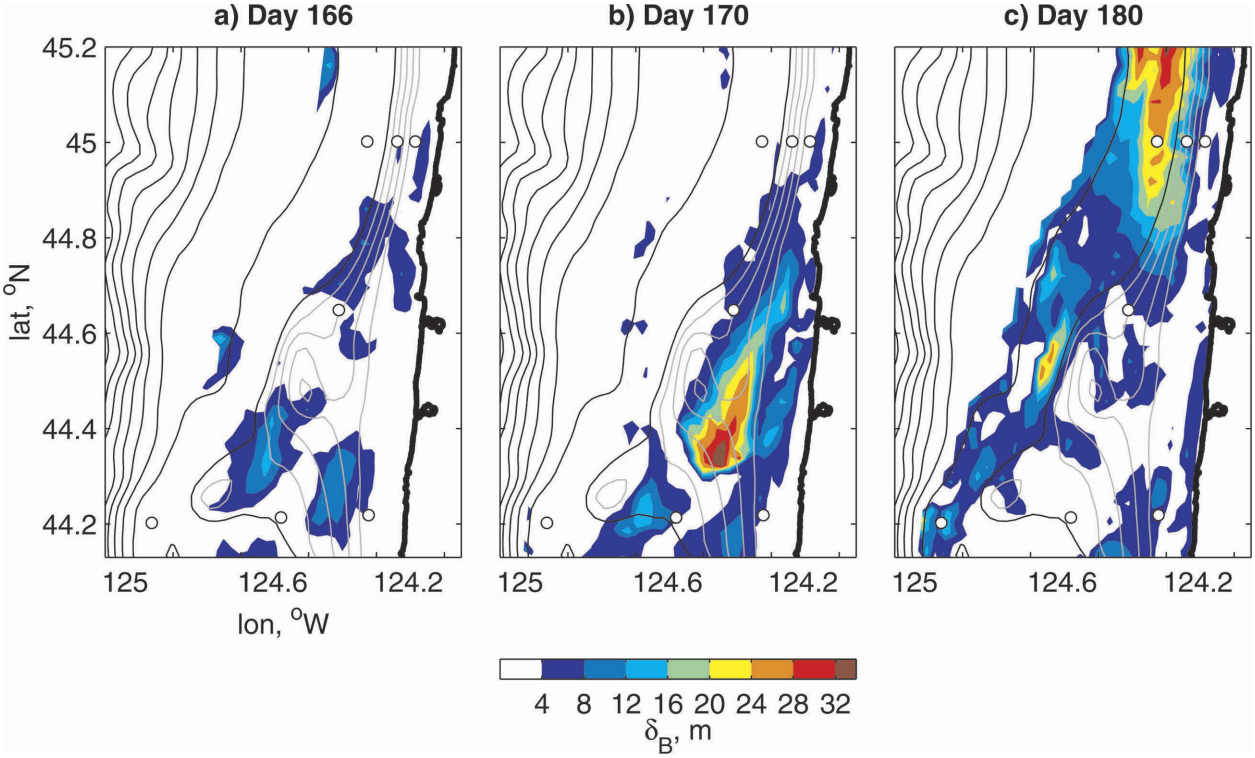

FIG. 9. Maps of daily averaged bottom mixed layer thickness δ_B (shown for shelf depths <250 m): (a) day 166 (near the peak of the upwelling-favorable wind), (b) day 170 (maximum BML thickness east of Stonewall Bank), (c) day 180 (maximum BML thickness at 45°N). Bathymetric contour intervals are 100 m for the black lines and 10 m (from 60 to 90 m) for the half-tone lines. Circles show mooring locations.

Averaged over the entire study period, w_p is generally low in the study area, with maximum average values near 3 m day^{-1} on the midshelf between latitudes 44.5° and 44.8°N and in the passage between Stonewall and Perpetua Banks. However, w_p may be significantly larger in response to events of increased southward wind stress. During these events, when pumping occurs for a sufficient period of time (e.g., more than a day), areas of larger w_p match closely those of larger δ_B. For instance, this can be seen in maps of w_p averaged over days 166 and 170 (Figs. 10a,b), where dashed black contours of $\delta_B = 12$ m are plotted over color-filled contours of w_p. On day 166 (Fig. 10a), near the peak of the upwelling-favorable wind, both w_p and δ_B are low in the area between the mooring lines, except for a spot near 44.3°N between Stonewall and Perpetua Banks, where $w_p > 14$ m day^{-1}. On day 170 (Fig. 10b), when δ_B is maximum east of Stonewall Bank, w_p is in excess of 10 m day^{-1} there. The areas of increased δ_B and $w_p > 0$ are both found on the inshore side of the upwelling jet that has separated from the coast. Note that increased w_p on day 170 is obtained both in the DA and model only solutions. The DA solution provides a more conservative estimate of the magnitude of pumping.

Plots of w_p as a function of x and t are shown in two cross sections in Fig. 11. Section locations are shown in Fig. 10a. Section A is drawn through the location near Stonewall Bank where the time series of δ_B has been analyzed (see Fig. 4b). Section B is located 14 km north of section A. The reasons to provide the analysis in two sections are to verify how robust the identified features are, and to obtain additional information about spatial variability of the studied process. During events of intensified pumping, δ_B is generally larger in section A than B, while w_p is larger in section B. For reference, time series of δ_B for selected locations in these cross sections are shown on the top of color plots of $w_p(x, t)$ in Fig. 11 (a δ_B curve for section A repeats that in Fig. 4b). Periods of increased w_p match closely periods of intensive δ_B growth, such that times of occurrence of maximum δ_B follow those of maximum w_p. Lagged correlation coefficients between w_p and δ_B for time series at the two selected locations in sections A and B are shown in Fig. 12. The maximum correlations are 0.54 (section A) and 0.67 (section B), achieved at the lags of

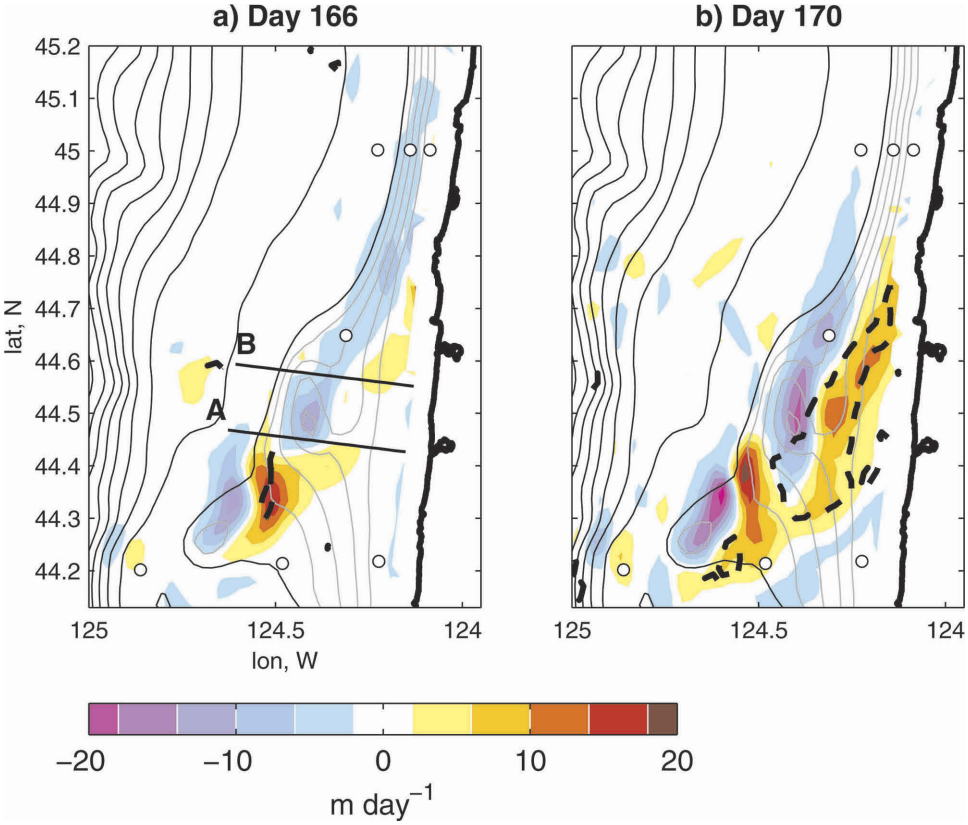

FIG. 10. Daily averaged bottom Ekman pumping velocity w_p (m day^{-1}): (a) day 166 and (b) day 170. Thick dashed contours show the BML thickness of 12 m, repeated from Fig. 9a,b. Bathymetric contour intervals are 100 m for the black lines and 10 m (from 60 to 90 m) for the gray lines. Circles show mooring locations. Lines A and B show section locations with reference to Fig. 11.

4 and 8 h, respectively, with δ_B lagging. In these correlation plots, there is clear asymmetry with respect to the maximum correlation point, such that the correlations are larger for the positive lags (consistent with the variability in w_p leading that in δ_B).

In the area east of Stonewall Bank, the pumping velocity is a significant contributor to the total vertical velocity in the BBL. To illustrate this, the time series of w_p is compared with that of the total vertical velocity in Cartesian coordinates $w(z_1)$ sampled at the selected locations in A and B (Fig. 13). For this analysis, w is taken at the time-varying distance of $0.8\delta_B(t)$ from the bottom, such that $z_1(t) = -H + 0.8\delta_B(t)$. This is close to the top of the BML, but, as will be shown later, below the layer of intensive convective mixing. Ideally for this analysis, w should be taken at the top of the BBL, which does not necessarily coincide with the top of the BML. However, we anticipate that BBL and BML thicknesses would be close since turbulence is increased throughout the BML, unrestricted by stratification (see discussion with reference to Fig. 17 below). In Fig. 13, $w(z_1)$ and w_p are indeed of comparable magnitude. For instance, during days 165–171, the maximum w_p is approximately one-half of the maximum w at the location in section A (Fig. 13a), and is as large as w at the location in section B (Fig. 13b). To help to substantiate the relationship between w and w_p, we also estimate the pumping velocity approximately as the difference of $w(z_1)$ and $w_{\text{topo}}(z_1) = -\mathbf{u}(z_1) \cdot \nabla H$, where $\mathbf{u} = (u, v)$, such that w_{topo} is the proxy for the component of w associated with inviscid flow over the topography. The plot of $w - w_{\text{topo}}$ is shown in Fig. 13 (dashed line) matching w_p (black solid line) in magnitude and variability. The correlation coefficients between these two time series are 0.49 (section A) and 0.62 (section B), which are high considering the number of assumptions leading to our interpretation of w_p and $w - w_{\text{topo}}$. To show that magnitudes and variability in w and its components near the top of the BML at the two selected locations are comparable over the entire study period, the means and standard deviations of the respective time series are given in Table 1.

To confirm the convective driving mechanism for enhanced mixing in the area of our focus, production

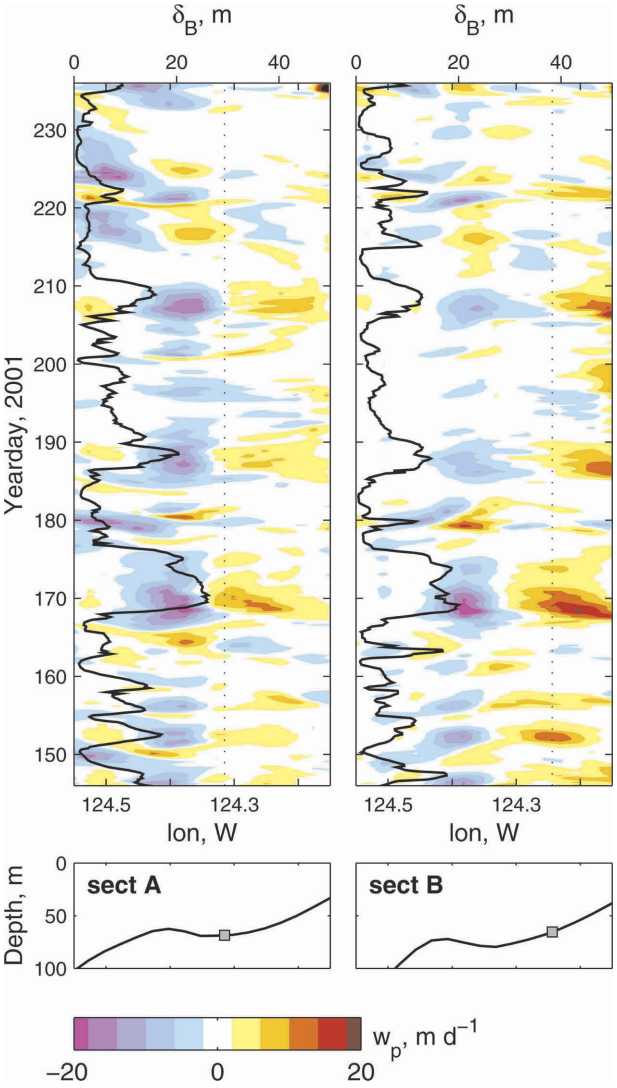

FIG. 11. Near-bottom pumping velocity w_p in cross-shore sections A and B (see Fig. 10a for section locations) shown as a function of longitude and time (upper plots, colored). Bathymetric depths in these sections are shown in lower panels. Black lines in upper plots are the BML thickness time series (DA solution) at the locations shown as dotted lines in the upper plots and squares in the lower plots.

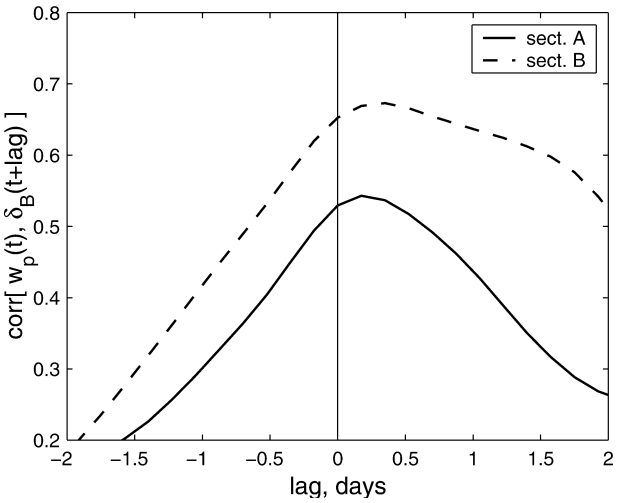

FIG. 12. Lagged correlation of the pumping velocity $w_p(t)$ and the BML thickness $\delta_B(t + \text{lag})$ at locations in sections A and B marked as squares in Fig. 11, days 146–237.

terms in the turbulent kinetic energy (TKE) equation are analyzed next. The shear production term is

$$P_{\text{SHEAR}} = K_M\left[\left(\frac{\partial u}{\partial z}\right)^2 + \left(\frac{\partial v}{\partial z}\right)^2\right], \tag{2}$$

and the buoyancy production term is

$$P_{\text{BUOY}} = \frac{gK_H}{\rho_o}\frac{\partial \sigma_\theta}{\partial z}, \tag{3}$$

where g is gravity, and K_M and K_H are the eddy viscosity and eddy diffusivity coefficients, respectively. For details of computation of K_M and K_H, see Wijesekera et al. (2003). Note that P_{SHEAR} is always positive, while $P_{\text{BUOY}} > 0$ only if stratification is unstable ($\partial\sigma_\theta/\partial z > 0$).

Averages of these terms for day 166 are shown in Fig. 14. In this figure, upper plots are maps of production terms on the model σ layer, at the depth of $0.96H(x, y)$. Lower plots show the corresponding terms in vertical section A (near 44.5°N). As upwelling develops, the near-bottom TKE shear production is increased along the path of the upwelling jet. However, since the upslope Ekman buoyancy transport increases stratification, buoyancy production is negative almost everywhere in this energetic area. Very close to the coast, positive P_{BUOY} is associated with overturning the water upwelled and transported offshore near the surface. On the midshelf, the magnitude of the near-bottom P_{BUOY} is about 10% of P_{SHEAR}, consistent with findings of Wijesekera et al. (2003) who showed that this picture can be considered typical of upwelling on the shelf slope. The total TKE production $P_{\text{SHEAR}} + P_{\text{BUOY}}$ is positive, but is confined to a relatively thin BBL, where it is largely balanced by the turbulent dissipation (see Wijesekera et al. 2003).

On day 170 (Fig. 15), shear production is still increased on the mid- and inner shelf, since upwelling continues. In contrast to day 166, the buoyancy production term is positive in the area east of Stonewall Bank, almost exactly where $\delta_B > 12$ m. Across the jet path, there is a sharp boundary between areas of negative and positive P_{BUOY}. Where $P_{\text{BUOY}} < 0$, the BML thick-

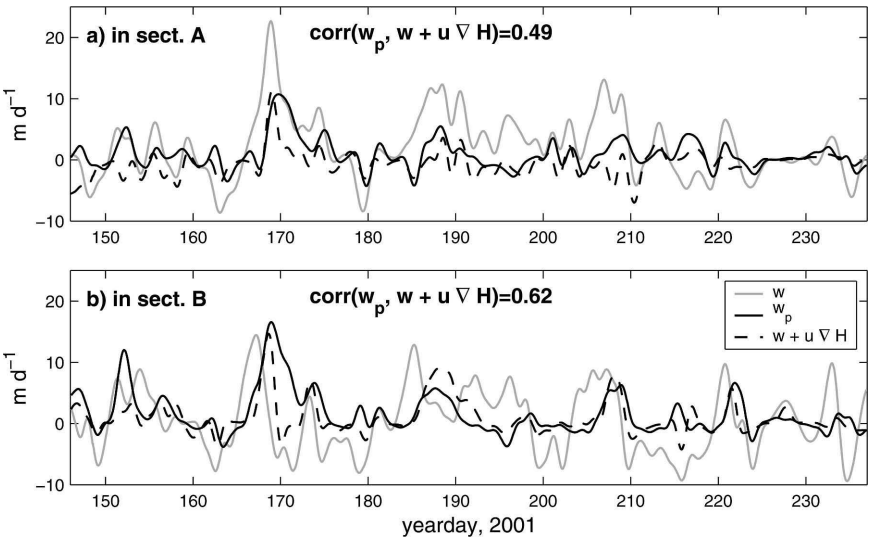

FIG. 13. Time series of low-pass-filtered pumping velocity w_p (black solid line), total vertical velocity $w(z_1)$ (gray line), and $w(z_1) + \mathbf{u}(z_1) \cdot \nabla H$ (dashed line), where w and $\mathbf{u}$ are at a time-varying distance of $0.8\delta_B$ from the bottom [such that $z_1(t) = -H + 0.8\delta_B(t)$]. Plots (a) and (b) are for the locations marked as squares in Fig. 11 in sections A and B, correspondingly.

ness is low, even though P_{SHEAR} is elevated there. In the vertical section of P_{BUOY} (Fig. 15d), the unstable layer rises 20 m above the bottom.

In Fig. 16a, contours of the near-bottom σ_θ averaged over day 170 are shown in vertical section B every 0.02 kg m^{-3} for $\sigma_\theta \geq 26$ kg m^{-3}. In this section plot, contour $\sigma_\theta = 26.4$ kg m^{-3} is thick, showing a pool of dense water raised 20 m above the bottom where w_p is maximum (Fig. 16b). It can be seen that the stratification is unstable here, especially clear in contours of σ_θ near the BML top on the offshore side of the w_p maximum. Gray profiles in Fig. 16a show horizontal velocities projected onto the section direction. Note bottom Ekman transport convergence, with near-bottom cross-shore velocities approaching zero in the area of maximum w_p. The dark shade background in Fig. 16a shows zones where the vertical gradient in the horizontal velocity exceeds 0.01 s^{-1}. Comparison of the density profiles and information on the velocity shear at the top of BML supports our hypothesis on the mechanism of increased mixing east of Stonewall Bank. The dense upwelled water is pumped up because of Ekman transport convergence. Then the vertically sheared horizontal currents displace the dense water near the top of BML, causing unstable density profiles that result in convectively driven mixing.

TABLE 1. The means and std devs (days 146–237) of the vertical velocity and its components estimated near the top of the BML at the two selected locations in sections A and B and plotted in Fig. 13.

	w_p	$w(z_1)$	$w(z_1) - w_{\mathrm{topo}}(z_1)$	$w_{\mathrm{topo}}(z_1)$
Section A, mean	0.89	2.14	−0.56	2.70
Section A, std dev	2.42	5.16	2.06	4.53
Section B, mean	1.57	0.39	0.94	−0.55
Section B, std dev	3.47	5.28	2.83	4.93

As a result of this process, the TKE in the BML east of Stonewall Bank is increased on day 170 relative to day 166, as can be seen in Fig. 17 showing the daily averaged $q^2 = 2 \times$ TKE in vertical cross-shore sections near 45° and 44.5°N (section A). On day 170, q^2 east of Stonewall Bank (Fig. 17d) is more than twice its magnitude on day 166 (Fig. 17c) and is enhanced in a larger water volume. Note that the surface boundary layer is thicker on day 170 (Fig. 17b) than on day 166 (Fig. 17a), since upwelling-favorable winds persisted during those days. At the same time, the BBL apparently gets thinner at 45°N as upwelling progresses. On both days, the maximum model alongshore surface current at 45°N is near 0.8 m s^{-1}. However, on the mid- and inner shelf near 45°N, the bottom stress magnitude on day 170 is only half its value on day 166, consistent with the theory of "slippery" BBL (MacCready and Rhines 1993). For our presentation, it is important to note that since q^2 is reduced near 45°N between days 166 and 170, the gain in the TKE east of Stonewall Bank on day 170 is more likely to be produced locally over the bottom convergence zone than be advected into that area.

To quantify the relative importance of convergence (advection) of near-bottom cold well-mixed water in the BML and local convective mixing in the support of

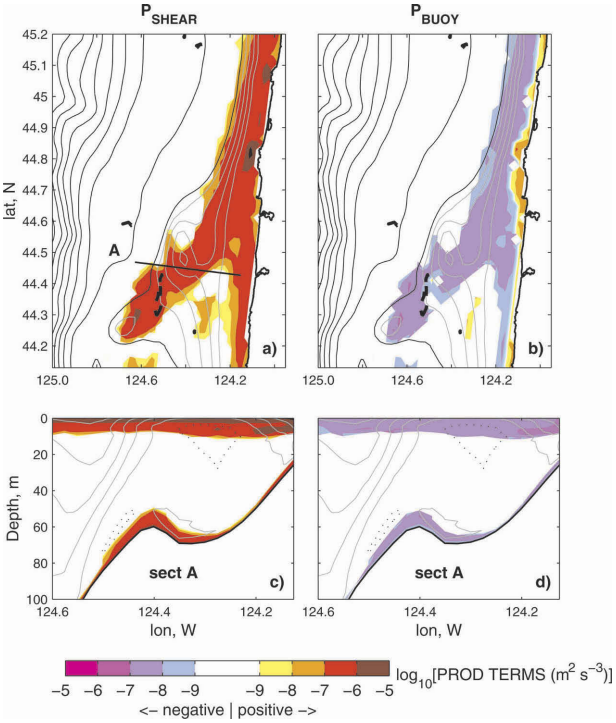

FIG. 14. Production terms in the TKE equation averaged over day 166 (near the peak of the upwelling-favorable wind stress), shear production is on the left and buoyancy production on the right. (top) The terms at the depth of 0.96*H*. (bottom) Cross-shore sections near Stonewall Bank at 44.5°N (section A). Bathymetric contour intervals in the top are 100 m for the black lines and 10 m (from 60 to 90 m) for the gray lines. In the bottom, contours are alongshore velocity, each 0.1 m s^{-1}, the dotted line is 0, and the gray lines are for the southward velocity. Thick dashed contours in (top) are of the daily averaged $\delta_B = 12$ m.

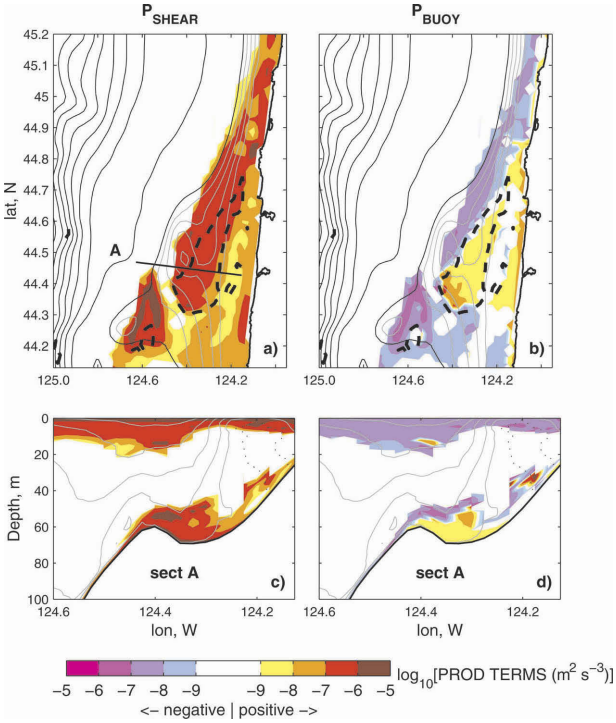

FIG. 15. Same as Fig. 14, but for day 170, when δ_B east of Stonewall Bank is maximum.

the large BML thickness east of Stonewall Bank, we perform an analysis of term balances in the temperature equation, written symbolically as

$$\frac{\partial T}{\partial t} = -\text{Advection} + \text{Horizontal Diffusion} + \frac{\partial}{\partial z}\left(K_H \frac{\partial T}{\partial z}\right) - \frac{\partial R}{\partial z}, \quad (4)$$

where T is the potential temperature, t is time, and R is the shortwave radiation flux. The horizontal diffusion is small and it is combined in the analysis with the advection term. Since the effect of penetrative heat flux is small near the bottom, the third and forth terms on the rhs of (4) are combined and referred to as the vertical diffusion term. Figure 18 shows the variability of the temperature and the terms in (4) as a function of z and t at a location east of Stonewall Bank, marked with the square at 44.45°N in Fig. 1a (which is the same location as that selected in section A, Fig. 11). In Fig. 18a, showing $T(z, t)$, the water column is cooled during days 168–172, with middepth isoterms progressively raised. Accordingly, the tendency term (Fig. 18b) is negative in most of the water column during those days, and is balanced by the sum of advection and vertical diffusion terms (Figs. 18c,d, respectively). On a log scale, the advection and vertical diffusion terms are comparable near the bottom.

The vertical advection term $-w\partial T/\partial z$, where w is the vertical velocity in Cartesian coordinates, is shown in Fig. 18e. It is a component of the total advection term, shown in Fig. 18c. In the BML, the vertical advection is very small since $\partial T/\partial z \approx 0$. The upper boundary of this layer is shown as the dashed line in Figs. 18b–e, for reference. Below this line, cooling or heating is uniform with depth (see Fig. 18b), largely balanced by the advection term. Both the vertical diffusion and advection terms are negative in the BML during the period of its intensive growth (days 168–172), providing cooling. However, beginning on day 169, in a thin layer at the top of the BML, the vertical diffusion is positive. In the same layer, the negative total advection is enhanced, relative to its values in the BML below, and the vertical component of advection is positive such that net cooling in this layer is provided solely by the horizontal advection. Such a balance at the top of the BML is consistent with the conceptual mechanism of the BML

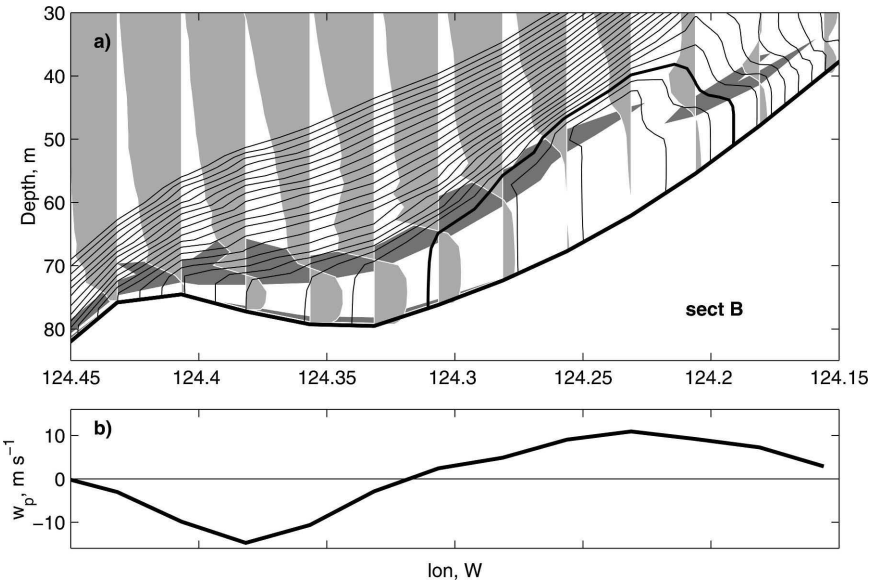

FIG. 16. (a) Contours of the potential density $\sigma_\theta \geq 26.0$ kg m^{-3} (black) and profiles of the velocity component (light tone) in the direction along the section line, section B (see Fig. 10a), averaged over day 170. Density contour interval is 0.02 kg m^{-3}. Contour $\sigma_\theta = 26.4$ kg m^{-3} is thick. The dark shade background shows areas of the magnitude of the vertical shear in horizontal velocity >0.01 s^{-1}; (b) Ekman pumping velocity w_p in the same section, averaged over the same day.

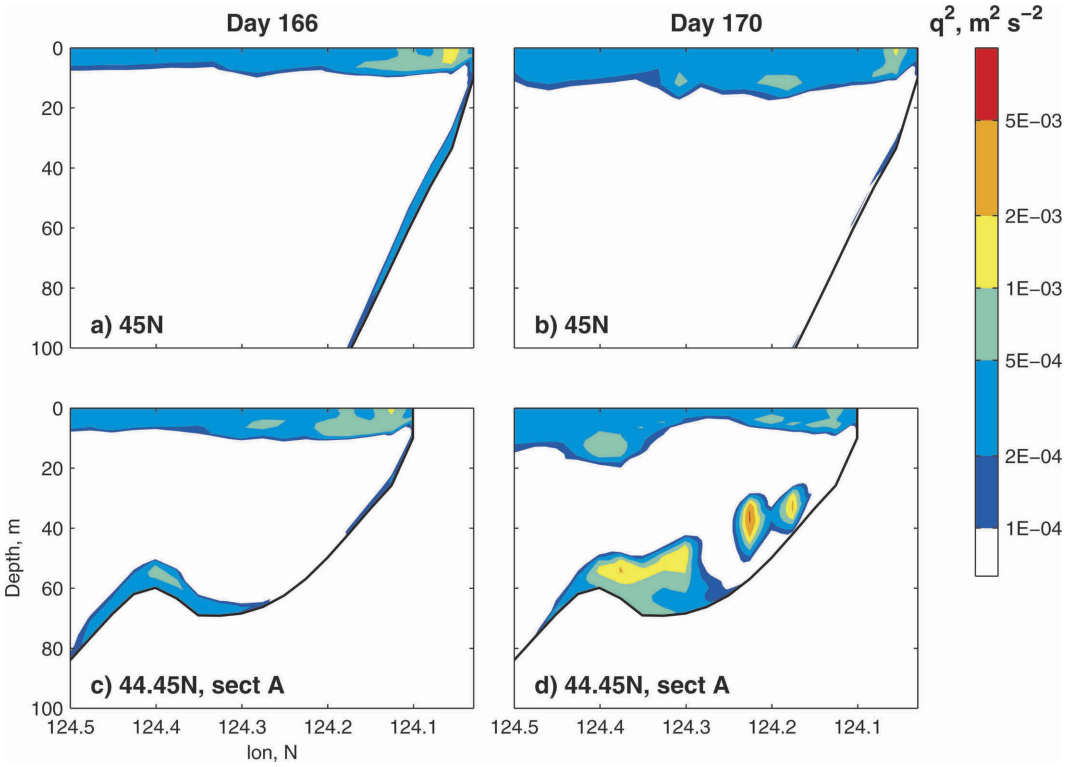

FIG. 17. Twice the turbulent kinetic energy q^2 in vertical cross-shore sections averaged over days (left) 166 and (right) 170. (top) Section near 45°N; (bottom) section near 44.45°N (section A, as in Figs. 14c,d and 15c,d). Note the log scale for contours.

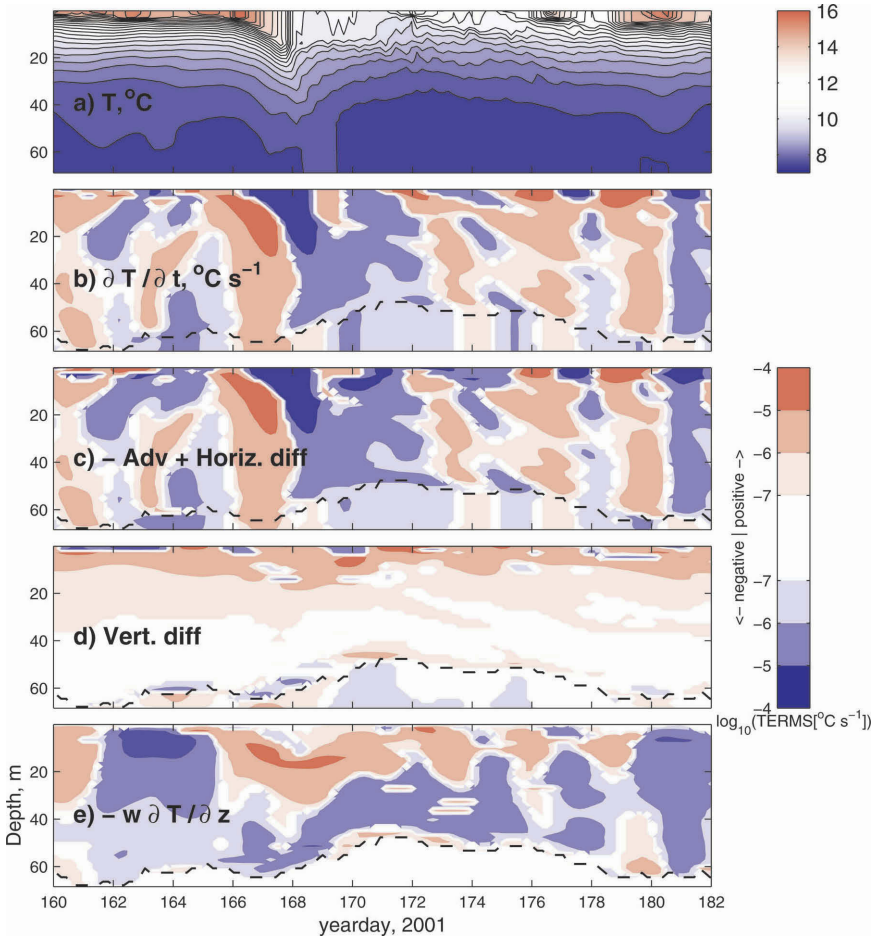

FIG. 18. Variability (vertical and time) of T and terms in the temperature Eq. (4) at the location east of Stonewall Bank (marked as square in Fig. 1a): (a) temperature, contour interval is 0.4°C, (b) tendency term, (c) minus total advection and horizontal diffusion terms combined, (d) vertical diffusion term, and (e) minus vertical advection. Note that term (b) is the sum of (c) and (d), and (e) is a component of (c). The dashed line shows the vertical extent of the bottom mixed layer.

growth described above. The negative sign of the horizontal advection is associated with the displacement of cold water at the top of the BML over a neighboring water column (e.g., see Fig. 16). In the model, unstable stratification results in increased K_H and vertical mixing that provides warming of the water patch at the top of the BML and moderate cooling below. In the layer at the top of the BML, $\partial T/\partial z < 0$ and $w > 0$ (see Fig. 13a) resulting in a positive vertical advection term on the rhs of (4).

Figure 19 provides more detailed information on the temperature equation balances at the same location, showing vertical profiles of the temperature and the tendency, advection, and vertical diffusion terms averaged for day 170. As seen in the temperature plot (Fig. 19a), the BML thickness is in excess of 20 m. In most of the BML, negative advection (thin solid line in Fig. 19b) accounts for 50%–90% of the tendency (bold solid line), with the rest of cooling provided by the vertical mixing (dashed line). The negative advection term is of relatively larger magnitude at the top of the BML, where it is balanced by correspondingly large positive vertical diffusion. As a result of the term balance analysis in (4), it is apparent that both horizontal advection and vertical mixing make important contributions to the processes that determine the BML thickness east of Stonewall Bank.

Figure 20 shows plots of the daily averaged near-bottom horizontal velocities and σ_θ for days 166–170. These identify the source of the dense bottom water east of Stonewall Bank (44.5°N). By day 170, a tongue of dense water approaches the area between the bank and the coast from the northwest, as indicated by the shape of the σ_θ = 26.4 kg m^{-3} contour and by the

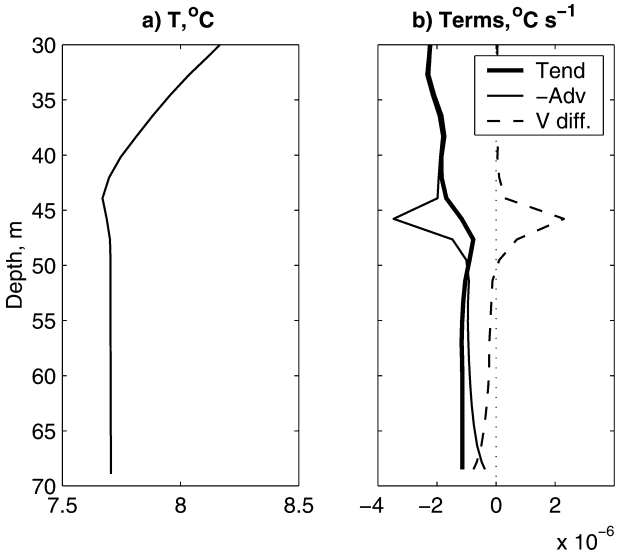

FIG. 19. Vertical profiles of (a) temperature, and (b) terms in the temperature equation at the location east of Stonewall Bank (marked as square in Fig. 1a), average on day 170.

bottom velocity vectors. Note that in the model, started from a state of rest with horizontally uniform stratification, water of this density was initially at a depth of 147 m. Vectors of horizontal bottom velocity for days 166 and 167 (Figs. 20a,b) show a relatively uniform upwelling over the mid- and inner shelf between 44.5° and 45°N. However, in plots for days 168, 169, and 170 (Figs. 20c,d,e) bottom velocity convergence is evident in that area, which can be associated with enhanced bottom Ekman pumping.

The growth of the BML is illustrated in two additional vertical sections, in which contours of daily averaged σ_θ are shown for a series of days 166–170 (Fig. 21). The section locations are shown in Fig. 20. Section C is in the approximate direction of the bottom current north of Stonewall Bank during these days. Density contours in this section (plots on the left in Fig. 21) show upslope advection of dense bottom water and the rising of isopycnals over the bottom toward the southern end of the section on days 169 and 170. Section D is chosen along the line of increased Ekman pumping. Density contours in this section (plots on the right in Fig. 21) show low BML thickness on day 166, associated with the development of upwelling across the line of this section, and the growth of the BML all along the section line in the following days reflecting the results of bottom Ekman pumping.

5. Implications

The present study demonstrates that under realistic conditions, bottom Ekman transport convergence may initiate near-bottom mixing, enhanced turbulence, and significant BML thickness growth in the shallow areas on the shelf. Several methods have been employed to quantify the intensity of the described phenomenon, including calculation of the bottom curl stress, analysis of the production terms in the TKE equation, and evaluation of term balances in the temperature equation. We anticipate that this mechanism may be active in places where an alongshore jet separates from the coast and flows over regions of a wider shelf. Also, increased bottom stress curl and Ekman pumping may result from near-bottom flow around small bathymetric features on the shelf, for example, as seen in a spot between Stonewall and Perpetua Banks (cf. map in Fig. 1a, currents in Fig. 3a, and w_p in Fig. 10).

Further studies are necessary to assess the ecological importance of the phenomenon found in the model east of Stonewall Bank. Can this mechanism affect the biological life locally and remotely, or the material transport in a larger area? Upwelling brings water rich in nutrients, but low in oxygen. Significant hypoxic events during summers of 2002 and 2004, associated with anomalously strong upwelling during those summers, caused migration of fish and death of crabs over a large, commercially important area of the mid-Oregon shelf (Wheeler et al. 2003). Comparative modeling studies for different years would be necessary to see whether the bottom Ekman transport convergence was stronger and more persistent in 2002 and 2004 than in 2001 and whether it played a critical role in the mentioned events. If the Ekman pumping persists at the rate of $w_p = 15$ m day^{-1} for several days, as in our modeling study, near-bottom nutrients may possibly be upwelled over the midshelf near Stonewall Bank to levels of about 30–40 m below the surface. Mixing at the top of the BML may provide an efficient mechanism for the BML material entrainment into the jet core. So, while the nutrients would probably not be pumped close enough to the euphotic zone (upper 20 m) to be taken up by phytoplankton locally, they could be uplifted and then advected with the alongshore jet, to be utilized farther to the south. To properly address these issues, detailed analyses of Lagrangian trajectories and of a coupled physical–biological model are needed.

There are indications that the BBL communicates with the surface boundary layer as a result of the bottom Ekman pumping. For instance, as can be seen in sections C and D (Fig. 21), the surface mixed layer experiences spatially uniform growth during the beginning of the upwelling event (days 166–167), but later appears to be locally suppressed by the near-surface

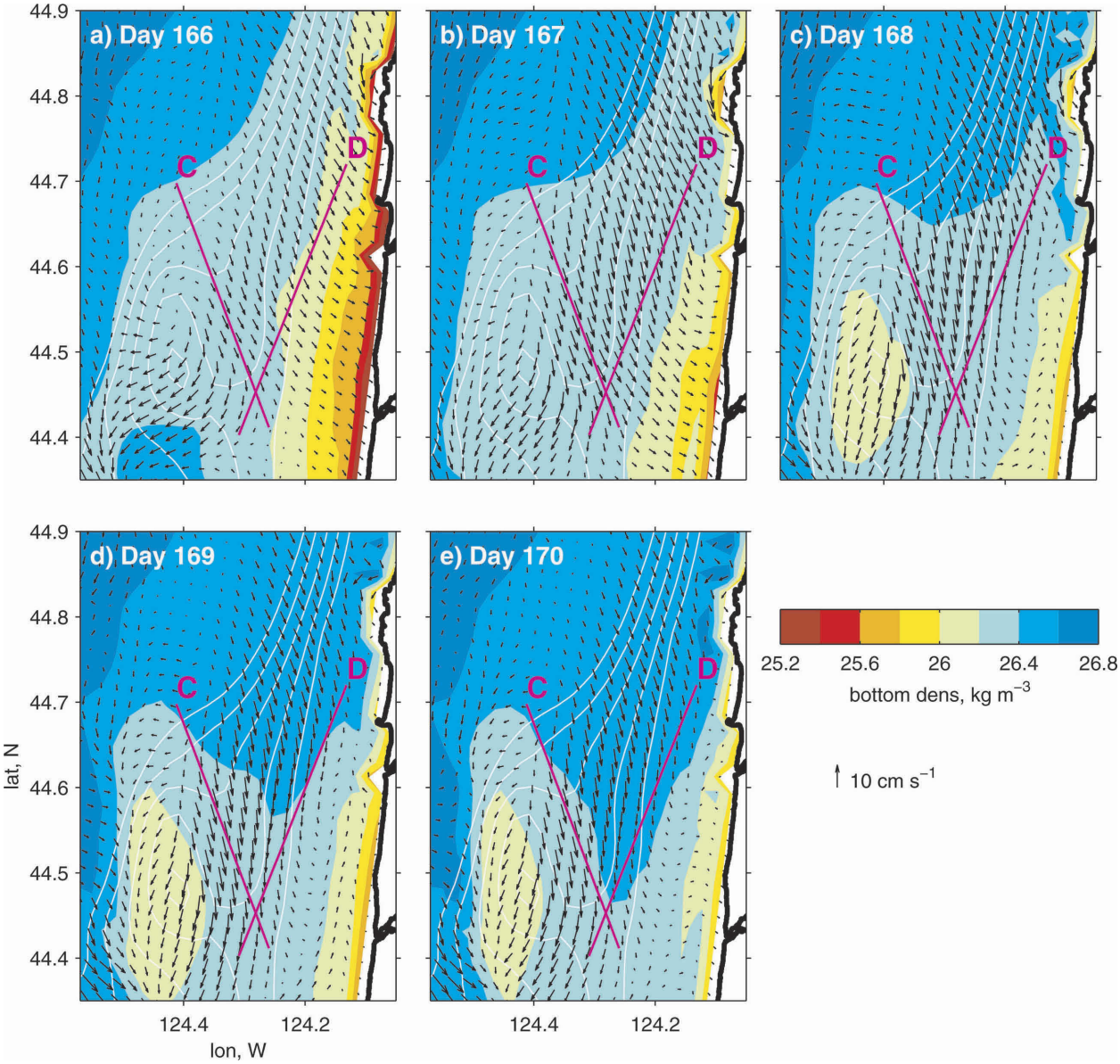

FIG. 20. Daily averaged bottom horizontal velocity and bottom σ_θ, days 166–170. Bathymetric contour intervals are 10 m (from 60 to 100 m). Lines C and D show section locations with reference to Fig. 21.

stratification east of Stonewall Bank (44.45°N). As a result of this, the surface turbulent BBL becomes thinner (cf. Figs. 17b,d). It is also possible that uplifting of the near-surface isopycnals in this area triggers baroclinic frontal instability. Horizontal resolution of our model (2 km) should be improved to establish this connection. A 1-km-resolution model of Durski and Allen (2005) resolves frontal instabilities with the wavelength of 8 km, which eventually evolve to larger spatial scales, significantly affecting the near-surface cross-shore material transport in a large area.

6. Summary

The analysis of the solution from a data-assimilative coastal ocean circulation model shows that bottom Ekman pumping creates conditions for increased, convectively driven bottom mixing on the midshelf east of Stonewall Bank off Oregon. In the area of the simple bathymetric slope, at latitude 45°N, and in the area 50 km to the south, on a wider shelf, different mechanisms govern variability in the BML thickness in response to upwelling- and downwelling-favorable conditions.

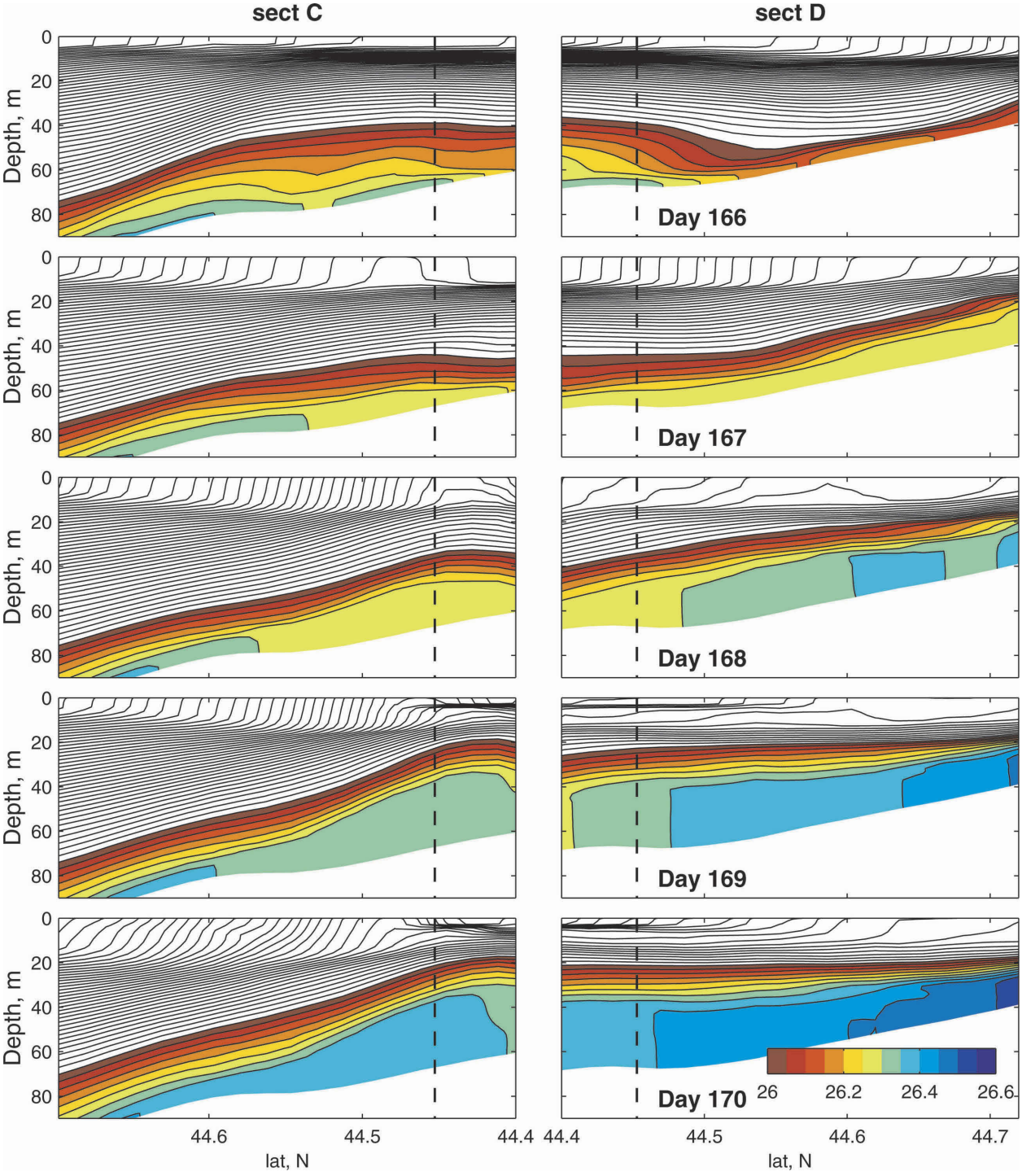

FIG. 21. Daily averaged σ_θ in vertical sections (left) C and (right) D, days 166–170. Section locations are shown in Fig. 20. The contour interval is 0.05 kg m^{-3}. Contours of $\sigma_\theta > 26$ kg m^{-3} are color filled. The vertical dashed line shows intersection of planes C and D.

When the BML thickness is large east of Stonewall Bank, it is low at 45°N, and vice versa. The maximum values of the BML thickness are comparable in these two areas, with occurrences of $\delta_B > 20$ m.

The bottom stress curl is used here as an indicator of the intensity of bottom Ekman pumping. Divided by ρ_o and f, it provides an estimate of the BBL contribution to the vertical velocity at the top of BBL, and

of the rate of change of the vertical distance between fluid parcels and the bottom, resulting from transport convergence in the BBL. While the bottom stress curl field is difficult to obtain from measurements, it is readily available as an output from the numerical model.

In the present case, model horizontal velocities are constrained by assimilation of moored velocity profiles in the shelf area spanning 90 km in the alongshore direction. Extensive model verification with respect to independent (not assimilated) data in a preceding study by Kurapov et al. (2005b) has increased confidence that the DA solution represents BBL variability better than the solution without DA at least during upwelling conditions. In this study, we saw that moored velocity data assimilation controls the level and the timing of periods of maximum of δ_B (see Figs. 4b,d).

Based on the interpretation of the upwelling case presented here, a question may be asked whether the situation reverses in downwelling conditions with the BBL convergence zone and increased BML thickness on the offshore side of the alongshore jet. During our study period, the impact of Ekman pumping on the BML thickness in response to downwelling could not be clearly demonstrated, in part because events of northward, downwelling-favorable winds were relatively short. For instance, in response to a significant northward wind event, the pumping velocity average on day 179 reached 6–12 m day^{-1} over bathymetric depths of 100–150 m in the area between 44.7° and 45°N, north of Stonewall Bank. However, the pumping velocity in that area was much smaller ($w_p < 6$ m day^{-1}) the preceding and following days. Note that these estimates are obtained from the solution without data assimilation since our data assimilation solution may possibly be less adequate during downwelling conditions than during upwelling conditions (for the reason explained in the end of section 2).

The present analyses have been focused on the area east of Stonewall Bank (44.5°N), and on the contrast between BML behavior there and in the area near 45°N. In the course of this study, several other areas of intensified mixing have also been identified. In particular, variability in the BBL near Heceta Bank around 44.1°N should be interesting to address in more detail in future studies.

Acknowledgments. This research was supported by the Office of Naval Research Ocean Modeling and Prediction Program under Grant N00014-98-1-0043, the National Science Foundation (NSF) Coastal Ocean Processes program under Grant OCE-9907854, and the NSF GLOBEC Program under Grant OCE-0000733. The authors are thankful to the two anonymous reviewers for their insightful comments.

REFERENCES

Barth, J. A., S. D. Pierce, and R. M. Castelao, 2005: Time-dependent, wind-driven flow over a shallow mid-shelf submarine bank. *J. Geophys. Res.,* in press.

Blumberg, A. F., and G. L. Mellor, 1987: A description of a three-dimensional coastal ocean circulation model. *Three-Dimensional Coastal Ocean Models*, N. Heaps, Ed., Coastal and Estuarine Science Series, Vol. 4, Amer. Geophys. Union, 1–16.

Boyd, T., M. D. Levine, P. M. Kosro, S. R. Gard, and W. Waldorf, 2002: Observations from moorings on the Oregon Continental Shelf, May–August 2001. Oregon State University Data Rep. 190, Ref. 2002-6, 196 pp.

Chase, Z., A. van Geen, P. M. Kosro, J. Marra, and P. A. Wheeler, 2002: Iron, nutrient, and phytoplankton distributions in Oregon coastal waters. *J. Geophys. Res.,* **107,** 3174, doi:10.1029/2001JC000987.

Durski, S. M., and J. S. Allen, 2005: Finite-amplitude evolution of instabilities associated with the coastal upwelling front. *J. Phys. Oceanogr.,* **35,** 1606–1628.

Galperin, B., L. H. Kantha, S. Hassid, and A. Rosati, 1988: A quasi-equilibrium turbulent energy model for geophysical flows. *J. Atmos. Sci.,* **45,** 55–62.

Gan, J., and J. S. Allen, 2005: Modeling upwelling circulation off the Oregon coast. *J. Geophys. Res.,* in press.

Garrett, C., P. MacCready, and P. Rhines, 1993: Boundary mixing and arrested Ekman layers: Rotating stratified flow near a sloping boundary. *Annu. Rev. Fluid Mech.,* **25,** 291–323.

Kurapov, A. L., J. S. Allen, G. D. Egbert, R. N. Miller, P. M. Kosro, M. Levine, and T. Boyd, 2005a: Distant effect of assimilation of moored currents into a model of coastal wind-driven circulation off Oregon. *J. Geophys. Res.,* **110,** C02022, doi:10.1029/2003JC002195.

——, and Coauthors, 2005b: Assimilation of moored velocity data in a model of coastal wind-driven circulation off Oregon: Multivariate capabilities. *J. Geophys. Res.,* in press.

Lentz, S. J., and J. H. Trowbridge, 1991: The bottom boundary layer over the northern California shelf. *J. Phys. Oceanogr.,* **21,** 1186–1201.

MacCready, P., and P. B. Rhines, 1993: Slippery bottom boundary layers on a slope. *J. Phys. Oceanogr.,* **23,** 5–22.

Mellor, G. L., and T. Yamada, 1982: Development of a turbulent closure model for geophysical fluid problems. *Rev. Geophys.,* **20,** 851–875.

Moum, J. N., A. Perlin, J. M. Klymak, M. D. Levine, T. Boyd, and P. M. Kosro, 2004: Convectively driven mixing in the bottom boundary layer. *J. Phys. Oceanogr.,* **34,** 2189–2202.

Nash, J. D., and J. N. Moum, 2001: Internal hydraulic flows on the continental shelf: High drag states over a small bank. *J. Geophys. Res.,* **106** (C3), 4593–4612.

Oke, P. R., J. S. Allen, R. N. Miller, G. D. Egbert, and P. M. Kosro, 2002a: Assimilation of surface velocity data into a primitive equation coastal ocean model. *J. Geophys. Res.,* **107,** 3122, doi:10.1029/2000JC000511.

——, and Coauthors, 2002b: A modeling study of the three-dimensional continental shelf circulation off Oregon. Part I: Model–data comparisons. *J. Phys. Oceanogr.,* **32,** 1360–1382.

——, J. S. Allen, R. N. Miller, and G. D. Egbert, 2002c: A modeling study of the three-dimensional continental shelf circulation off Oregon. Part II: Dynamical balances. *J. Phys. Oceanogr.,* **32,** 1383–1403.

Pedlosky, J., 1987: *Geophysical Fluid Dynamics.* Springer-Verlag, 710 pp.

Perlin, A., J. N. Moum, and J. M. Klymak, 2005: Response of the bottom boundary layer over a sloping shelf to variations in alongshore wind. *J. Geophys. Res.,* in press.

Trowbridge, J. H., and S. J. Lentz, 1991: Asymmetric behavior of an oceanic boundary layer above a sloping bottom. *J. Phys. Oceanogr.,* **21,** 1171–1185.

Wheeler, P. A., A. Huyer, and J. Fleischbein, 2003: Cold halocline, increased nutrients and higher chlorophyll off Oregon in 2002. *Geophys. Res. Lett.,* **30,** 8012, doi:10.1029/2003GL017395.

Wijesekera, H. W., J. S. Allen, and P. A. Newberger, 2003: Modeling study of turbulent mixing over the continental shelf: Comparison of turbulent closure schemes. *J. Geophys. Res.,* **108,** 3103, doi:10.1029/2001JC001234.